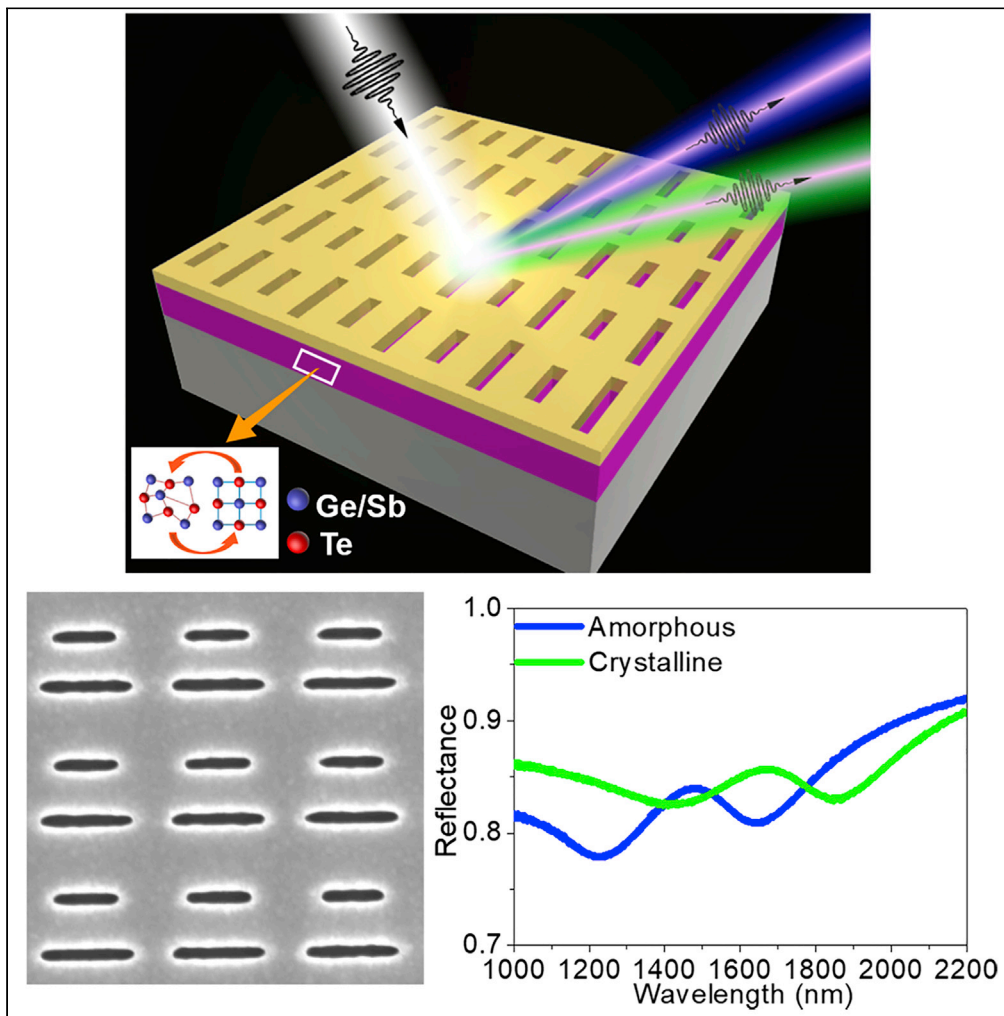**Article**

Tuning of Classical Electromagnetically Induced Reflectance in Babinet Chalcogenide Metamaterials

Kuan Liu, Yang Li, Kairong Qin, Tun Cao

caotun1806@dlut.edu.cn

HIGHLIGHTS

Tunable electromagnetically induced reflectance (EIR) metamaterial

The EIR is created by hybridization of two dipolar modes of paired metal slots

Article

Tuning of Classical Electromagnetically Induced Reflectance in Babinet Chalcogenide Metamaterials

Kuan Liu,[1,2] Yang Li,[1] Kairong Qin,[1] and Tun Cao[1,2,3,*]

SUMMARY

Metamaterials analog of electromagnetically induced reflectance (EIR) has attracted intense attentions since they can provide various applications for novel photonic devices such as optical detectors with a high sensitivity and slow-light devices with a low loss. The development of dynamic photonic devices desires a tunable EIR feature in metamaterials. However, most metamaterials-induced EIR is not spectrally controllable particularly for the near-infrared (NIR) region. Herein, a tuning of EIR is illustrated in Babinet chalcogenide metamaterials in the NIR region. The EIR response is created by weak hybridization of two dipolar (bright) modes of the paired Au slots. Such a mode interference can be engineered through non-volatile phase transition to the refractive index of the $Ge_2Sb_2Te_5$ (GST), resulting in an active controlling of the reflection window. A 15% spectral tuning of the reflectance peak is observed experimentally in the NIR region as switching the GST state between amorphous and crystalline.

INTRODUCTION

Electromagnetically induced transparency (EIT) is an elimination of absorption, originally existing in atomic medium and stemming from quantum interference (Boller et al., 1991). It allows for a very narrow transparency window for wave transmitting through an originally opaque medium (Harris, 1997). To clearly observe the EIT in the quantum system, the sample needs to be kept under cryogenic temperature (Fleischhauer et al., 2005) under two coherent laser sources. This phenomenon was later mimicked using plasmonic metamaterials (Athe et al., 2018; Chu et al., 2018; Gu et al., 2012; Habib et al., 2018; Krishnamoorthy et al., 2020; Lari et al., 2020; Liu et al., 2009a, 2011, 2012; Papasimakis et al., 2008; Qin et al., 2020; Singh et al., 2009; Song et al., 2019a, 2019b; Song and Zhang, 2020; Tassin et al., 2009; Vafapour, 2017, 2019; Vafapour and Forouzeshfard, 2017; Vafapour and Ghahraloud, 2018; Verellen et al., 2009; Zhang et al., 2008; Zhong et al., 2020) that operated at room temperature with incoherent light source.

The analog of EIT in metamaterials depends on a Fano-type interaction (Fano, 1961; Luk'yanchuk et al., 2010) achieved by either the weak hybridization of two bright modes (Liu et al., 2008; Zhang et al., 2008) or the destructive interference between bright and dark modes (Fedotov et al., 2007; Kekatpure et al., 2010; Papasimakis et al., 2008). However, these EIT metamaterials work in the transmission mode thus requiring transparent substrate, which forbids the design wavelengths based on the kind of substrates being employed (Hokmabadi et al., 2015; Zhang et al., 2017; Zhu et al., 2013). In this regard, an EIT-like response in the reflectance spectra so-called electromagnetically induced reflectance (EIR) will be more talented for improving photonic device efficiency. So far, few works devote attention to the EIR metamaterials (Chun-Feng et al., 2014; Guo et al., 2017) and only operate at a fixed frequency, which hampers their applications. On the other hand, it shows that the EIT metamaterials can be tuned by integrating the various active materials such as metal hydrides (Strohfeldt et al., 2014), graphene (Cheng et al., 2013), vanadium dioxide (Duan et al., 2013), and liquid crystals (Decker et al., 2013). Yet, the actively tunable EIR metamaterials have not been studied. Moreover, these tuning approaches tend to be not practical in the near-infrared (NIR) region because the active materials exhibit a strong Drude contribution to the permittivity. The NIR regime is, whereas, a key spectrum having atmospheric transparency window, optical telecommunication wavelengths, or molecular vibrational fingerprints (Agrawal, 2012; Stanley, 2012; Tittl et al., 2015; Yin et al., 2015).

Since explored in the 1960s (Ovshinsky, 1968), chalcogenide semiconductor phase change materials (PCMs) have attracted intense attention owing to their significant portfolio of properties (Gao and Bao, 2020; Shportko et al., 2008; Simpson et al., 2011; Wuttig et al., 2017). In particular, it has been shown that the structural rearrangement in the chalcogenide semiconductor can be switched by electrical (Wang et al., 2008) or optical (Salinga et al., 2013) pulses, offering nonvolatile and optical (e.g., DVD-RW) phase-change random access memory devices (Iwasaki et al., 1993; Kwon et al., 2011). Furthermore, the prompt amorphous-to-crystalline phase change in the most studied PCMs, $Ge_2Sb_2Te_5$ (GST), makes it superlative for active photonic devices (Behera et al., 2017; Cao et al., 2013a, 2013b, 2017; Hosseini et al., 2014; Karvounis et al., 2016; Li et al., 2016; Mkhitaryan et al., 2017; Waldecker et al., 2015; Wuttig et al., 2017; Zhou et al., 2016). Recently, the switchable photonic devices have been realized by transiting the state of GST225 (Chen and Song, 2019; Kalikka et al., 2016; Wang et al., 2016; Wei et al., 2019; Zhou et al., 2017). It is because that the GST permittivity exhibits a vast change in the optical region during the phase transition (Michel et al., 2013, 2014).

Herein, we illustrate experimentally that plasmonically induced reflectance (PIR) can be tuned by using planar complementary hybrid metal-GST metamaterials in the NIR regime. Based on Babinet's theory (Liu et al., 2008; Zentgraf et al., 2007), we propose the metamaterials made of cut-out antenna in the Au-GST stacked films, where a reflectance peak is induced instead of transmittance peak. To excite the PIR phenomena, coherently coupled bright and bright modes are introduced. A pair of slot dipolar resonators with the different lengths, which are efficiently coupled to light, supports two different bright modes. A weak hybridization of the two bright modes results in the PIR features. We further experimentally present that GST amorphous-crystalline phase transition offers a significant reflectance contrast at the resonance and hence tune the reflected light frequency, in which a resonant wavelength of peak reflectance varies from $\lambda = 1{,}470$–$1{,}670$ nm. The experiment matches well with the calculation. The cut-out scheme can be easily realized by nanoimprint lithography or focused-ion-beam (FIB) writing and promising for the highly integrated NIR photonic devices (Liu et al., 2009b). The pronounced reflectance signal may be employed to measure the mass concentration for biomolecules, i.e., proteins, DNA, and glucose, which readily fills the voids and facilitates the sensing (Zhang et al., 2019).

RESULTS AND DISCUSSIONS

Figure 1A schematically illustrates the geometry of the Babinet metamaterial. It is formed from a periodic lattice made of two asymmetric slots in a 40-nm-thick Au film ($T_{Au} = 40$ nm) on a 30-nm-thick GST dielectric layer ($T_{GST} = 30$ nm). Herein, the Au is chosen as the metal film owing to its advantages of non-oxidation, excellent chemical stability, and low loss in the NIR region (West et al., 2010). A 5-nm-thick silicon nitride (Si_3N_4) diffusion barrier is deposited between the Au and GST layers, which can prevent the interlayer diffusion and interfacial reactions (Chew et al., 2017). The metamaterials reside on a silicon (Si) substrate. The gap between the two horizontal cut-out (the nanoslit dipolar resonators) is $d = 200$ nm. The lengths of the double nanoslit are $l_1 = 250$ and $l_2 = 350$ nm, respectively, while maintaining the width at $w = 50$ nm. The periods along x and y axes are $P_x = P_y = 500$ nm. The Babinet metamaterials can excite the plasmonic bright modes, where a reflectance maximum can be approximated by using the geometry (slots) of the complementary features of the Au asymmetric double nanorods. The Babinet metamaterial is fabricated by FIB writing, where the field-emission scanning electron microscopy (SEM) image of the sample is shown in Figure 1B. The sample is of 100 μm × 100 μm area, possessing ~40,000 individual meta-atoms. The GST layer is deposited onto a Si substrate. Radio frequency sputtering system is employed to deposit the GST and Si_3N_4 layers under argon (Ar) atmosphere at room temperature (see Transparent Methods for detail). In contrast to the other devices that exhibit optical switching of chalcogenide semiconductor with nanosecond pulsed laser (Pandian et al., 2006; Salinga et al., 2013), our Au-GST stacked layers are very thin (~1/25 of the operating wavelength) and avoid using the capping layer. The employment of the capping layer not only increases the losses from metamaterials but decreases the resonance move by enlarging the distance between the metamaterials and the GST film. Figure 1C illustrates the complex refractive index of a 30-nm-thick monolithic GST film on a Si substrate for the different structural states of the amorphous (red lines) and crystalline (blue lines). Variable-angle spectroscopic ellipsometry (VASE) is used to measure the complex refractive index ($N_{GST} = n_{GST} + i \times k_{GST}$) that is subsequently fitted by a Tauc-Lorentz model (Sreekanth et al., 2018) in the spectral range from 1,000 to 2,200 nm. As is seen, there is a radical change in the spectra of the real part of the complex refractive index (n_{GST}) between the amorphous and crystalline states, which in turn produces the tunable NIR resonances. The variation of N_{GST} in the
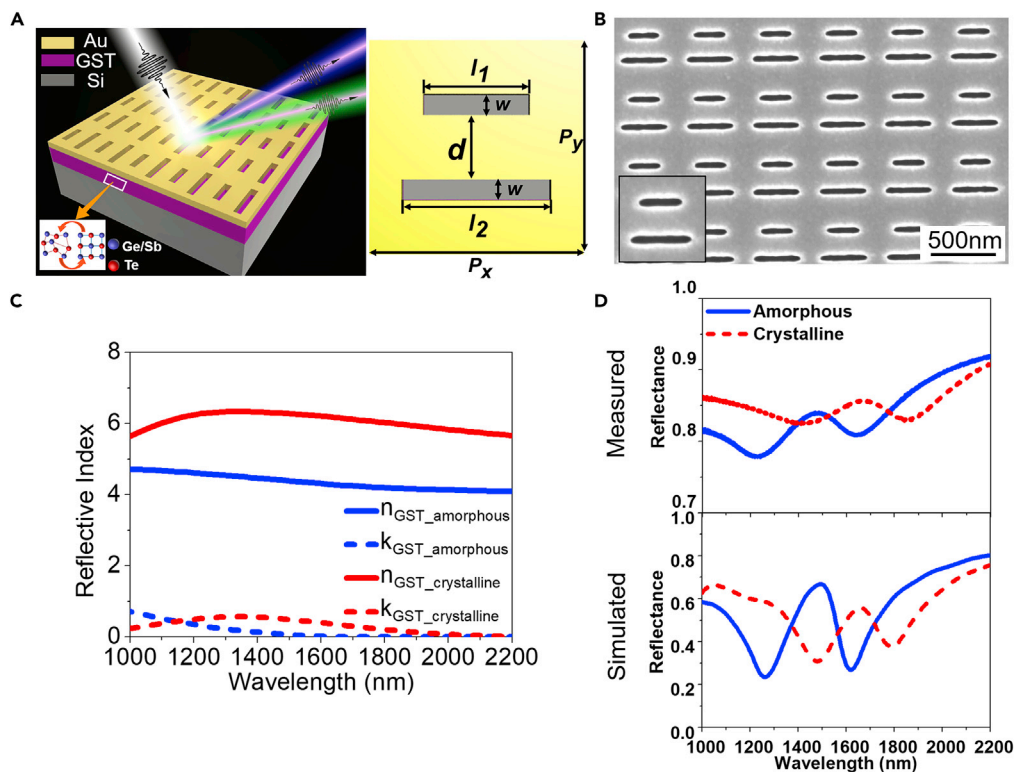
Figure 1. Configuration and Performance of the EIR Babinet Metamaterials

(A) Schematic illustration of the Babinet metamaterials. The geometrical parameters are: T_{Au} = 40 nm, T_{GST} = 30 nm, d = 200 nm, l_1 = 250, l_2=350 nm, w = 50 nm, and $P_x = P_y$ = 500 nm.

(B) SEM image of the fabricated metamaterials. Inset: zoom-in image of the unit cell.

(C) NIR complex refractive index of 30-nm-thick GST film for both as-deposited amorphous and thermal annealing crystalline phases, where the refractive index data were measured using ellipsometer over a spectral range of 1,000–2,200 nm.

(D) The FTIR measured (top panel) and FDTD simulated (bottom panel) reflectance spectra of the Babinet metamaterials for both the amorphous (blue solid lines) and crystalline (red dashed lines) phases under p-polarized incident light.

GST is owing to a bonding change from predominantly covalent in the amorphous state to resonant bonds in the crystalline state (Iwasaki et al., 1993).

Reflectance measurements for the different structural states are carried out by Fourier transform infrared (FTIR) spectroscopy via a 15× Cassegrain objective (NA = 0.4) and a liquid nitrogen cooled MCT detector (see Transparent Methods for detail). The metamaterials are under a normal incidence with p-polarization. The experimentally measured reflectance spectra are shown in the top panel of Figure 1D. Both nanoslots serve as dipolar antennae and are strongly excited by the p-polarized incident light, and the excited two bright modes interfere with each other. By breaking the symmetry of the paired slots, a tiny reflectance peak can be experimentally observed within the reflectance spectra. This is because the two resonant modes are weakly hybridized. Note that the gap between the two slots is fixed, so the coupling strength is determined by the difference in the length between the two slots, leading to the splitting of resonant mode. Namely, the EIR characteristic is caused by the weak hybridization of the two bright modes with frequency detuning (Fu et al., 2016). As transiting the structural state of the GST from amorphous (blue solid line) to crystalline (red dashed line), the reflectance peak endures a wavelength redshift of 200 nm, while maintaining a reflectance peak of ∼0.85. Therefore, the device reflectance can switch between two spectrally separate NIR bands. Herein, the crystallization of GST layer is achieved by thermally annealing the as-deposited amorphous film for 30 min at 180°C on a hotplate in a flowing Ar atmosphere. The numerically simulated transmittance spectra have a qualitative agreement with the experimentally measured one.
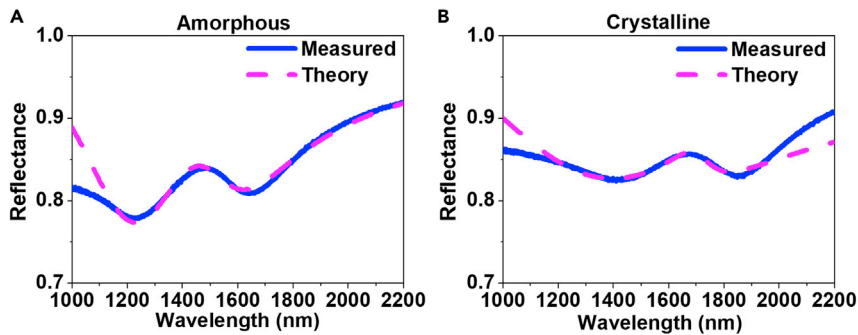
Figure 2. Theoretical Fitting of the Measured Data
The FTIR measured (blue solid lines) and theoretically fitted (magenta dashed lines) reflectance spectra of the Babinet metamaterials with (A) amorphous and (B) crystalline phases. The metamaterials are normally illuminated under *p*-polarized incident light.

The finite-difference time-domain (FDTD) calculations performed with the commercial software package Lumerical Solutions software are presented on the bottom panel of Figure 1D for comparison. In the model, the GST refractive index is obtained from the VASE measured data from Figure 1C. The Au permittivity was taken from Johnson and Christy's data (Johnson and Christy, 1972). The metamaterials were modeled under normal incident plane wave with *p*-polarization. A plane wave source along the *-z* axis is used to illuminate the metamaterials possessing the electric field component (*E*-) parallel to the *x* axis. The metamaterial geometry is set to that measured using the SEM pictures shown in Figure 1B. A detailed model's explanation is shown in the Methods. A redshift in the resonant peak occurs by crystallizing the GST. In the model, we do not take into account the Si_3N_4 adhesion layer, fabrication imperfections (i.e., the inhomogeneity of the gap separation), native oxides, and surface roughness. This simplification can cause the variation between the simulated and measured reflected intensity and the slight widening of the measured spectra. On the other hand, in the simulations, the reflectance is calculated in the near-field of the metamaterials. Nevertheless, the reflectance is measured in the far-field over a finite acceptance angle within the 0.4 NA microscope objective light cone. This may also introduce differences between the simulation and the experiment.

To explore the origin of the actively tunable EIR response, the harmonic oscillator system is employed to quantitatively analyze the coupling between the two nanoslits (Joe et al., 2006).Herein, the EIR feature appears due to the interaction between two dipole (bright) modes of the paired Au slots. Such a mode interference can be engineered through non-volatile phase transition to the refractive index of the GST, resulting in an active controlling of the reflection window. The motion of oscillating charges for each mode can be expressed using the coupled differential equations,

$$\ddot{x}_1 + \gamma_1 \dot{x}_1 + \omega_1^2 x_1 + \kappa^2 x_2 = E \qquad \text{(Equation 1)}$$
$$\ddot{x}_2 + \gamma_2 \dot{x}_2 + \omega_2^2 x_2 + \kappa^2 x_1 = 0 \qquad \text{(Equation 2)}$$

where κ denotes the coupling coefficient between the two slots (Miroshnichenko et al., 2010);x_1,x_2, γ_1, and γ_2 represent the amplitudes and damping rates of the two dipole (bright) modes, respectively. The ω_1 and ω_2 are the resonant frequencies of the two bright modes, respectively. By solving the coupled Equations 1 and 2, the susceptibility χ of the metamaterials can be obtained (Luo et al., 2016; Xiao et al., 2018)

$$\chi = \chi_r + i\chi_i \propto \frac{\omega_2^2 - \omega^2 + i\gamma_2\omega}{(\omega_1^2 - \omega^2 + i\gamma_1\omega)(\omega_2^2 - \omega^2 + i\gamma_2\omega) - \kappa^4} \qquad \text{(Equation 3)}$$

Because the energy dissipation is proportional to χ_i, the reflectance can be theoretically calculated by

$$R = 1 - g\chi_i \qquad \text{(Equation 4)}$$

where *g* is a geometric parameter presenting the coupling strength of the bright mode with the incident *E*-field. In Figures 2A and 2B, we illustrate the analytical fitted reflectance spectra via the coupled harmonic oscillator model for both amorphous and crystalline states, respectively, exhibiting a very good agreement with the measured spectra.

	κ (THz)	γ_1 (THz)	γ_2 (THz)
Amorphous	91.5	92.9	11.8
Crystalline	58.5	71.6	12.5

Table 1. The Parameters κ, γ_1, and γ_2 Used in Fitting for the Different States

The corresponding fitting parameters for the different states are listed in Table 1. As is seen, γ_1 and γ_2 do not vary significantly, whereas the κ decreases sharply as transiting the state of GST from amorphous to crystalline. Therefore, the active tuning of the EIR resonance mainly stems from the variation in the κ.

Besides the active tuning of the EIR via the GST phase transition, the EIR response is also polarization selective in which "On" and "Off" states can be achieved by switching the incident light between the p- and s-polarizations. To further demonstrate the controlling of the spectra characteristic, in Figure 3 we both experimentally and numerically investigate the spectra evolution under the s-polarized incidence for amorphous (Figure 3A) and crystalline (Figure 3B) states. For the s-polarized incidence, the resonance in the metamaterials for both amorphous and crystalline states is not excited, the EIR response is faded away. On the contrary, for the p-polarized incidence (Figure 1D), the resonance in the metamaterials is excited and the EIR is observed. Our proposed chalcogenide metamaterials can act as tunable optical polarizer (Lin et al., 2017), where the "On" and "Off" states can be obtained in the different spectral bands. The polarization-selective EIR response possesses a good trend of the Malus law, which may open up new possibilities for programmable infrared metamaterial devices for on-chip photonic modulation and manipulation applications.

To better understand the fundamental physics, in Figures 4A–4C the calculated electric $E = \sqrt{E_x^2 + E_y^2 + E_z^2}$ field distributions of the paired nanoslits are shown for three resonant wavelengths of λ = 1,262, 1,490, and 1,620 nm for the amorphous state. The E-field distributions clearly present that both slots are excited individually at λ = 1,262 and 1,620 nm and act as the dipolar (bright) mode resonances. On the other hand, at λ = 1,490 nm, the EIR feature is obtained by the simultaneous excitation of the two slots, which validates that the EIR is mainly associated with the weak hybridization of two dipolar modes of the two Au slots. In Figures 4D–4F, we show the distributions of the E-field at the resonant wavelengths of λ = 1,480, 1,662, and 1,790 nm, respectively, for the crystalline phase. It can be observed that the E-field distributions are similar to the ones for the amorphous phase, which indicates that the electrical resonant dipoles in the two slots can be excited to create EIR response. The localized E-fields in the amorphous GST (Figures 4A–4C) are enhanced more strongly than for the crystalline state (Figures 4D–4F), implying that a greater interaction of the two bright modes can be achieved, which in turn leads to a sharper EIR profile.

To exploit the underlying forming process of the EIR characteristic, the two different slot dipolar resonators are separately fabricated and measured using the same processes as illustrated above. The first structure is made of the longer slots array whose SEM image is shown in Figure 5A. The experimentally measured reflectance spectra are shown in Figure 5B for the amorphous (blue solid lines) and crystalline (red dashed lines) states under the p-polarized incident wave. A redshift in the resonant dip is observed by crystallizing the GST. The second structure consists of the shorter slots array (Figure 5C). As was seen in Figure 5D, the resonant dip in the reflectance spectra redshifts to the longer wavelength as crystallizing the GST film while having a lower quality factor compared to the amorphous one. Note that the reflectance spectral profiles of the two different slots arrays are similar; thus, both the slots act as the bright modes. When the two slot resonators are integrated within a meta-atom and create the EIR Babinet metamaterials, a reflectance peak of 85% at λ = 1,470 nm appears between two resonant dips located at λ = 1,230 and 1,645 nm (blue solid lines in Figure 1D). This peak reflectance originates from the near field coupling between the two bright modes. By transiting the state from amorphous to crystalline, the resonant wavelength for the reflectance peak redshifts from λ = 1,470 to 1,670 nm (red dashed lines in Figure 1D).

In Figure 6, we have numerically simulated chalcogenide metamaterials based on the various metal films of Au, Ag, Al, and Cu as changing the GST state from amorphous (Figure 6A) to crystalline (Figure 6B). As is seen, the electromagnetically induced reflectance exists for all the different metals, whereas the metamaterials based on the Au film possess the largest spectral shift by crystallizing the as-deposited amorphous GST.
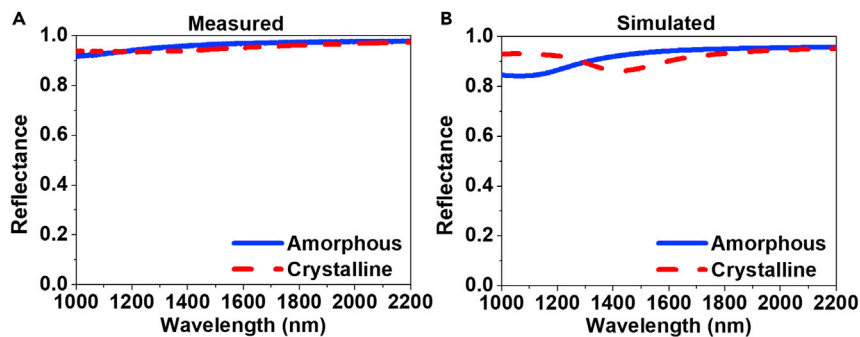
Figure 3. Performance of the Babinet Metamaterials under *s*-polarized Incidence
The (A) FTIR-measured and (B) FDTD-simulated reflectance spectra of the Babinet metamaterials for both the amorphous (blue solid lines) and crystalline (red dashed lines) phases under *s*-polarized incident light.

Conclusion

In conclusion, we have theoretically investigated and experimentally realized a tunable EIR response using the GST-based complementary Babinet metamaterials in the NIR region. By switching the structural phase of GST between amorphous and crystalline, the EIR peak is spectrally shifted. A massive tuning range from λ = 1,470 to 1,670 nm was demonstrated for the FTIR measurements of EIR metamaterials, which is also numerically validated. This is because the GST phase change offers a pronounced contrast in the refractive index. The EM-field distributions reveal that the EIR response originates from the weak hybridization of two dipolar (bright) modes of the paired Au slots. These findings may be used in many innovative areas such as nonlinear optics, high sensitivity detector, and slow-light applications.

Limitations of the Study

The quality factor of resonance peak of the Babinet metasurface is not very high. It is because the resonance peak is created by the weak hybridization of two bright modes of the paired Au slots. Further study will be needed to address this issue. The ultrashort laser pulse is an important part for a reversible tuning of the resonant modes in the Babinet metasurface. Future studies in reversible switching of the EIR under an
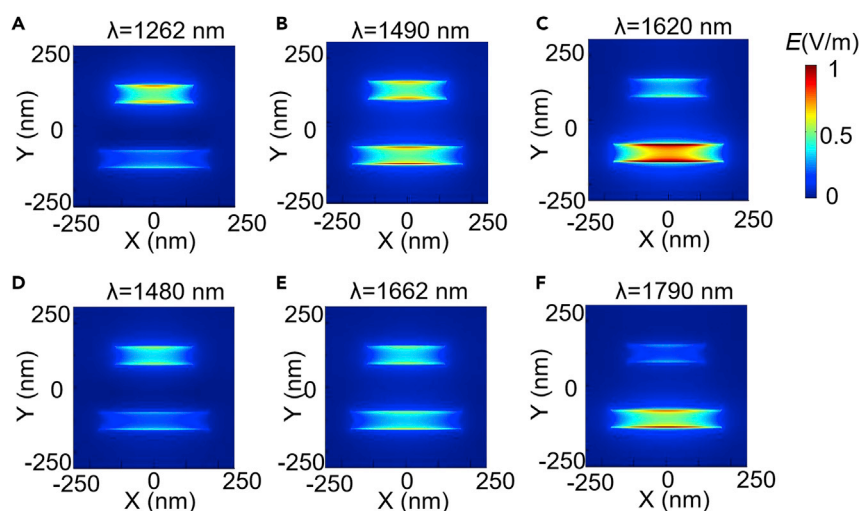

Figure 4. Electromagnetic Fields Distributions of the Babinet Phase Change Metamaterials under *p*-polarized Incidence
3D-FDTD simulation of total *E*-field intensity distributions for (A–C) amorphous metamaterials at the resonant wavelengths of (A) λ = 1,262 nm, (B) λ = 1,490 nm, (C) λ = 1,620 nm, and for (D–F) crystalline metamaterials at the resonant wavelengths of (D) λ = 1,480 nm, (E) λ = 1,662 nm, (F) λ = 1,790 nm.
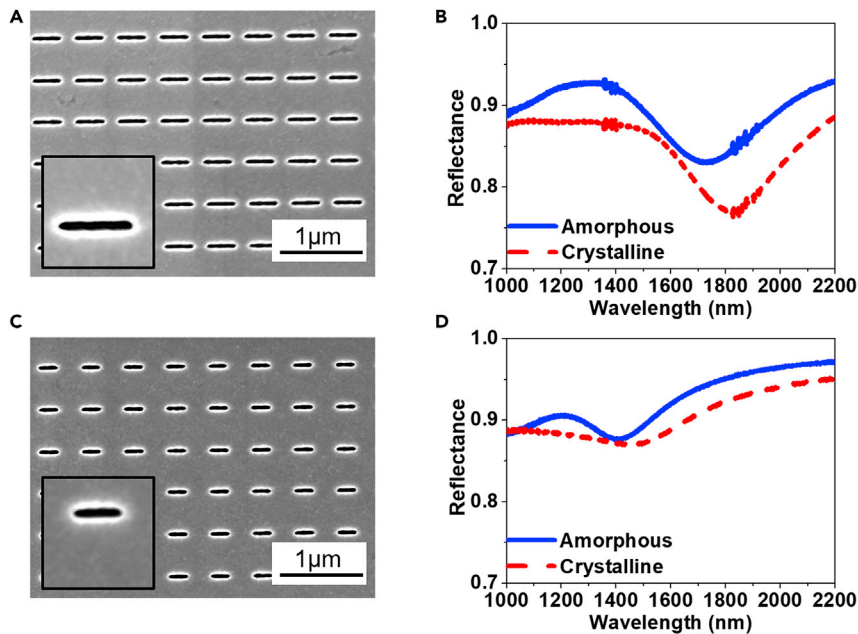
Figure 5. Forming Process of the EIR Response under *p*-polarized Incidence

(A and B) (A) SEM image and (B) measured reflectance spectra of the longer slots array with both amorphous (blue solid line) and crystalline (red dashed line) states.

(C and D) (C) SEM image and (D) measured reflectance spectra of the shorter slots array with both amorphous (blue solid line) and crystalline (red dashed line) states.

excitation of ultrashort pulsed laser can provide various applications for dynamically reconfigurable photonic devices, such as optical detectors and slow-light devices.

Resource Availability

Lead Contact

Further information and requests for resources should be directed to the Lead Contact, Tun Cao (caotun1806@dlut.edu.cn).

Materials Availability

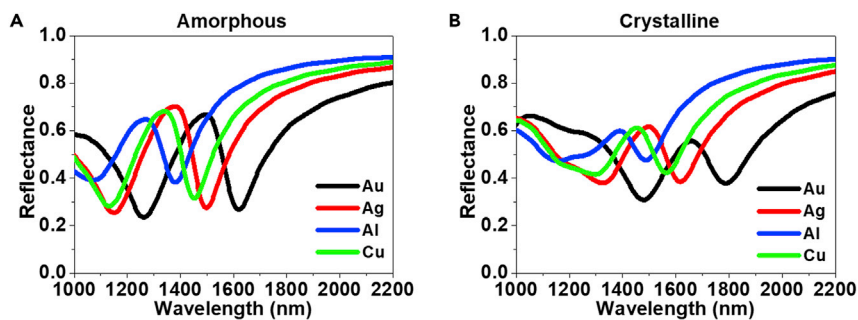No newly generated materials were generated during this study.

Figure 6. Effect of the Various Metals on the Spectra

The FDTD-simulated reflectance spectra of the Babinet metamaterials based on the various metal films of Au (black line), Ag (red line), Al (blue line), and Cu (green line) for both the (A) amorphous and (B) crystalline phases under *p*-polarized incident light.

METHODS

All methods can be found in the accompanying Transparent Methods supplemental file.

SUPPLEMENTAL INFORMATION

Supplemental Information can be found online at https://doi.org/10.1016/j.isci.2020.101367.

ACKNOWLEDGMENTS

AUTHOR CONTRIBUTIONS

Conceptualization, T.C.; Methodology, K.L.; Investigation, T.C., K.L., and Y.L.; Writing – Original Draft, T.C., K.Q., and K.L.; Writing – Review & Editing, T.C., K.Q., and K.L.; Resources, T.C. and K.Q.; Supervision, T.C.

DECLARATION OF INTERESTS

The authors declare no competing interests.

REFERENCES

Agrawal, G.P. (2012). Fiber-optic Communication Systems, *vol. 222* (John Wiley & Sons).

Athe, P., Srivastava, S., and Thapa, K.B. (2018). Electromagnetically induced reflectance and Fano resonance in one dimensional superconducting photonic crystal. Physica C Supercond. *547*, 36–40.

Behera, J.K., Zhou, X., Tominaga, J., and Simpson, R.E. (2017). Laser switching and characterisation of chalcogenides: systems, measurements, and applicability to photonics. Opt. Mater. Express *7*, 3741–3759.

Boller, K.-J., Imamoğlu, A., and Harris, S.E. (1991). Observation of electromagnetically induced transparency. Phys. Rev. Lett. *66*, 2593.

Cao, T., Li, Y., Wei, C.-W., and Qiu, Y.-M. (2017). Numerical study of tunable enhanced chirality in multilayer stack achiral phase-change metamaterials. Opt. Express *25*, 9911–9925.

Cao, T., Simpson, R.E., and Cryan, M.J. (2013a). Study of tunable negative index metamaterials based on phase-change materials. J. Opt. Soc. Am. B *30*, 439–444.

Cao, T., Wei, C., Simpson, R.E., Zhang, L., and Cryan, M.J. (2013b). Rapid phase transition of a phase-change metamaterial perfect absorber. Opt. Mater. Express *3*, 1101–1110.

Chen, A., and Song, Z. (2019). Wideband polarization-insensitive dielectric switch for mid-infrared waves realized by phase change material Ge3Sb2Te6. Europhys. Lett. *126*, 27004.

Cheng, H., Chen, S., Yu, P., Duan, X., Xie, B., and Tian, J. (2013). Dynamically tunable plasmonically induced transparency in periodically patterned graphene nanostrips. Appl. Phys. Lett. *103*, 203112.

Chew, L.T., Dong, W., Liu, L., Zhou, X., Behera, J., Liu, H., Sreekanth, K.V., Mao, L., Cao, T., and Yang, J. (2017). Chalcogenide active photonics. Paper presented at: Active photonic platforms IX (International Society for Optics and Photonics).

Chu, Q., Song, Z., and Liu, Q.H. (2018). Omnidirectional tunable terahertz analog of electromagnetically induced transparency realized by isotropic vanadium dioxide metasurfaces. Appl. Phys. Express *11*, 082203.

Chun-Feng, D., Ya-Ting, Z., Jian-Quan, Y., Chong-Ling, S., De-Gang, X., and Gui-Zhong, Z. (2014). Reflection-type electromagnetically induced transparency analogue in terahertz metamaterials. Chin. Phys. B *23*, 124203.

Decker, M., Kremers, C., Minovich, A., Staude, I., Miroshnichenko, A.E., Chigrin, D., Neshev, D.N., Jagadish, C., and Kivshar, Y.S. (2013). Electro-optical switching by liquid-crystal controlled metasurfaces. Opt. Express *21*, 8879–8885.

Duan, X., Chen, S., Cheng, H., Li, Z., and Tian, J. (2013). Dynamically tunable plasmonically induced transparency by planar hybrid metamaterial. Opt. Lett. *38*, 483–485.

Fano, U. (1961). Effects of configuration interaction on intensities and phase shifts. Phys. Rev. *124*, 1866.

Fedotov, V., Rose, M., Prosvirnin, S., Papasimakis, N., and Zheludev, N. (2007). Sharp trapped-mode resonances in planar metamaterials with a broken structural symmetry. Phys. Rev. Lett. *99*, 147401.

Fleischhauer, M., Imamoglu, A., and Marangos, J.P. (2005). Electromagnetically induced transparency: optics in coherent media. Rev. Mod. Phys. *77*, 633.

Fu, G.-L., Zhai, X., Li, H.-J., Xia, S.-X., and Wang, L.-L. (2016). Tunable plasmon-induced transparency based on bright-bright mode coupling between two parallel graphene nanostrips. Plasmonics *11*, 1597–1602.

Gao, S., and Bao, X. (2020). Chalcogenide taper and its nonlinear effects and sensing applications. iScience *23*, 100802.

Gu, J., Singh, R., Liu, X., Zhang, X., Ma, Y., Zhang, S., Maier, S.A., Tian, Z., Azad, A.K., and Chen, H.-T. (2012). Active control of electromagnetically induced transparency analogue in terahertz metamaterials. Nat. Commun. *3*, 1151.

Guo, B., Loo, Y., and Ong, C. (2017). Polarization independent and tunable plasmonic structure for mimicking electromagnetically induced

transparency in the reflectance spectrum. J. Opt. *19*, 105101.

Habib, M., Gokbayrak, M., Ozbay, E., and Caglayan, H. (2018). Electrically controllable plasmon induced reflectance in hybrid metamaterials. Appl. Phys. Lett. *113*, 221105.

Harris, S.E. (1997). Electromagnetically induced transparency. Phys. Today *50*, 36–42.

Hokmabadi, M.P., Philip, E., Rivera, E., Kung, P., and Kim, S.M. (2015). Plasmon-induced transparency by hybridizing concentric-twisted double split ring resonators. Sci. Rep. *5*, 15735.

Hosseini, P., Wright, C.D., and Bhaskaran, H. (2014). An optoelectronic framework enabled by low-dimensional phase-change films. Nature *511*, 206.

Iwasaki, H., Harigaya, M., Nonoyama, O., Kageyama, Y., Takahashi, M., Yamada, K., Deguchi, H., and Ide, Y. (1993). Completely erasable phase change optical disc II: Application of Ag-In-Sb-Te mixed-phase system for rewritable compact disc compatible with CD-velocity and double CD-velocity. Jpn. J. Appl. Phys. *32*, 5241.

Joe, Y.S., Satanin, A.M., and Kim, C.S. (2006). Classical analogy of Fano resonances. Phys. Scr. *74*, 259.

Johnson, P.B., and Christy, R.-W. (1972). Optical constants of the noble metals. Phys. Rev. B *6*, 4370.

Kalikka, J., Zhou, X., Behera, J., Nannicini, G., and Simpson, R.E. (2016). Evolutionary design of interfacial phase change van der Waals heterostructures. Nanoscale *8*, 18212–18220.

Karvounis, A., Gholipour, B., MacDonald, K.F., and Zheludev, N.I. (2016). All-dielectric phase-change reconfigurable metasurface. Appl. Phys. Lett. *109*, 051103.

Kekatpure, R.D., Barnard, E.S., Cai, W., and Brongersma, M.L. (2010). Phase-coupled plasmon-induced transparency. Phys. Rev. Lett. *104*, 243902.

Krishnamoorthy, H., Adamo, G., Yin, J., Savinov, V., Zheludev, N., and Soci, C. (2020). Infrared dielectric metamaterials from high refractive index chalcogenides. Nat. Commun. *11*, 1–6.

Kwon, Y., Kim, J., Chae, S., Lee, Y., Kim, S., Ku, J., Sohn, Y., Park, S., Choi, D., and Om, J. (2011). Device characteristics of a Ge-doped SbTe alloy for high-speed phase-change random access memory. J. Korean Phys. Soc. *59*, 466–469.

Lari, E.S., Vafapour, Z., and Ghahraloud, H. (2020). Optically tunable triple–band perfect absorber for nonlinear optical liquids sensing. IEEE Sens. J. *99*, 1.

Li, P., Yang, X., Maß, T.W., Hanss, J., Lewin, M., Michel, A.-K.U., Wuttig, M., and Taubner, T. (2016). Reversible optical switching of highly confined phonon–polaritons with an ultrathin phase-change material. Nat. Mater. *15*, 870.

Lin, H., Song, Y., Huang, Y., Kita, D., Deckoff-Jones, S., Wang, K., Li, L., Li, J., Zheng, H., and Luo, Z. (2017). Chalcogenide glass-on-graphene photonics. Nat. Photon. *11*, 798.

Liu, N., Hentschel, M., Weiss, T., Alivisatos, A.P., and Giessen, H. (2011). Three-dimensional plasmon rulers. Science *332*, 1407–1410.

Liu, N., Kaiser, S., and Giessen, H. (2008). Magnetoinductive and electroinductive coupling in plasmonic metamaterial molecules. Adv. Mater. *20*, 4521–4525.

Liu, N., Langguth, L., Weiss, T., Kästel, J., Fleischhauer, M., Pfau, T., and Giessen, H. (2009a). Plasmonic analogue of electromagnetically induced transparency at the Drude damping limit. Nat. Mater. *8*, 758.

Liu, N., Weiss, T., Mesch, M., Langguth, L., Eigenthaler, U., Hirscher, M., Sonnichsen, C., and Giessen, H. (2009b). Planar metamaterial analogue of electromagnetically induced transparency for plasmonic sensing. Nano Lett. *10*, 1103–1107.

Liu, X., Gu, J., Singh, R., Ma, Y., Zhu, J., Tian, Z., He, M., Han, J., and Zhang, W. (2012). Electromagnetically induced transparency in terahertz plasmonic metamaterials via dual excitation pathways of the dark mode. Appl. Phys. Lett. *100*, 131101.

Luk'yanchuk, B., Zheludev, N.I., Maier, S.A., Halas, N.J., Nordlander, P., Giessen, H., and Chong, C.T. (2010). The Fano resonance in plasmonic nanostructures and metamaterials. Nat. Mater. *9*, 707.

Luo, W., Cai, W., Xiang, Y., Wang, L., Ren, M., Zhang, X., and Xu, J. (2016). Flexible modulation of plasmon-induced transparency in a strongly coupled graphene grating-sheet system. Opt. Express *24*, 5784–5793.

Michel, A.-K.U., Chigrin, D.N., Maß, T.W., Schönauer, K., Salinga, M., Wuttig, M., and Taubner, T. (2013). Using low-loss phase-change materials for mid-infrared antenna resonance tuning. Nano Lett. *13*, 3470–3475.

Michel, A.-K.U., Zalden, P., Chigrin, D.N., Wuttig, M., Lindenberg, A.M., and Taubner, T. (2014). Reversible optical switching of infrared antenna resonances with ultrathin phase-change layers using femtosecond laser pulses. ACS Photon. *1*, 833–839.

Miroshnichenko, A.E., Flach, S., and Kivshar, Y.S. (2010). Fano resonances in nanoscale structures. Rev. Mod. Phys. *82*, 2257.

Mkhitaryan, V.K., Ghosh, D.S., Rudé, M., Canet-Ferrer, J., Maniyara, R.A., Gopalan, K.K., and Pruneri, V. (2017). Tunable complete optical absorption in multilayer structures including. Adv. Opt. Mater. *5*, 1600452.

Ovshinsky, S.R. (1968). Reversible electrical switching phenomena in disordered structures. Phys. Rev. Lett. *21*, 1450.

Pandian, R., Kooi, B.J., De Hosson, J.T.M., and Pauza, A. (2006). Influence of capping layers on the crystallization of doped Sb x Te fast-growth phase-change films. J. Appl. Phys. *100*, 123511.

Papasimakis, N., Fedotov, V.A., Zheludev, N., and Prosvirnin, S. (2008). Metamaterial analog of electromagnetically induced transparency. Phys. Rev. Lett. *101*, 253903.

Qin, F., Chen, Z., Chen, X., Yi, Z., Yao, W., Duan, T., Wu, P., Yang, H., Li, G., and Yi, Y. (2020). A tunable triple-band near-infrared metamaterial absorber based on Au nano-cuboids array. Nanomaterials *10*, 207.

Salinga, M., Carria, E., Kaldenbach, A., Bornhöfft, M., Benke, J., Mayer, J., and Wuttig, M. (2013). Measurement of crystal growth velocity in a melt-quenched phase-change material. Nat. Commun. *4*, 2371.

Shportko, K., Kremers, S., Woda, M., Lencer, D., Robertson, J., and Wuttig, M. (2008). Resonant bonding in crystalline phase-change materials. Nat. Mater. *7*, 653.

Simpson, R.E., Fons, P., Kolobov, A.V., Fukaya, T., Krbal, M., Yagi, T., and Tominaga, J. (2011). Interfacial phase-change memory. Nat. Nanotechnol. *6*, 501–505.

Singh, R., Rockstuhl, C., Lederer, F., and Zhang, W. (2009). Coupling between a dark and a bright eigenmode in a terahertz metamaterial. Phys. Rev. B *79*, 085111.

Song, Z., Chen, A., Zhang, J., and Wang, J. (2019a). Integrated metamaterial with functionalities of absorption and electromagnetically induced transparency. Opt. Express *27*, 25196–25204.

Song, Z., Chu, Q., Zhu, C., Chen, Q., and Wang, W. (2019b). Polarization-Independent terahertz tunable analog of electromagnetically induced transparency. IEEE Photon. Technol. Lett. *31*, 1297–1299.

Song, Z., and Zhang, B. (2020). Controlling wideband absorption and electromagnetically induced transparency via a phase change material. Europhys. Lett. *129*, 57003.

Sreekanth, K.V., Han, S., and Singh, R. (2018). Ge2Sb2Te5-Based tunable perfect absorber cavity with phase singularity at visible frequencies. Adv. Mater. *30*, 1706696.

Stanley, R. (2012). Plasmonics in the mid-infrared. Nat. Photon. *6*, 409.

Strohfeldt, N., Tittl, A., Schäferling, M., Neubrech, F., Kreibig, U., Griessen, R., and Giessen, H. (2014). Yttrium hydride nanoantennas for active plasmonics. Nano Lett. *14*, 1140–1147.

Tassin, P., Zhang, L., Koschny, T., Economou, E., and Soukoulis, C.M. (2009). Low-loss metamaterials based on classical electromagnetically induced transparency. Phys. Rev. Lett. *102*, 053901.

Tittl, A., Michel, A.K.U., Schäferling, M., Yin, X., Gholipour, B., Cui, L., Wuttig, M., Taubner, T., Neubrech, F., and Giessen, H. (2015). A switchable mid-infrared plasmonic perfect absorber with multispectral thermal imaging capability. Adv. Mater. *27*, 4597–4603.

Vafapour, Z. (2017). Near infrared biosensor based on Classical Electromagnetically Induced Reflectance (Cl-EIR) in a planar complementary metamaterial. Opt. Commun. *387*, 1–11.

Vafapour, Z. (2019). Polarization-independent perfect optical metamaterial absorber as a glucose sensor in Food Industry applications. IEEE Trans. Nanobioscience *18*, 622–627.

Vafapour, Z., and Forouzeshfard, M. (2017). Disappearance of plasmonically induced reflectance by breaking symmetry in metamaterials. Plasmonics *12*, 1331–1342.

Vafapour, Z., and Ghahraloud, H. (2018). Semiconductor-based far-infrared biosensor by optical control of light propagation using THz metamaterial. J. Opt. Soc. Am. B *35*, 1192–1199.

Verellen, N., Sonnefraud, Y., Sobhani, H., Hao, F., Moshchalkov, V.V., Dorpe, P.V., Nordlander, P., and Maier, S.A. (2009). Fano resonances in individual coherent plasmonic nanocavities. Nano Lett. *9*, 1663–1667.

Waldecker, L., Miller, T.A., Rudé, M., Bertoni, R., Osmond, J., Pruneri, V., Simpson, R.E., Ernstorfer, R., and Wall, S. (2015). Time-domain separation of optical properties from structural transitions in resonantly bonded materials. Nat. Mater. *14*, 991.

Wang, Q., Rogers, E.T., Gholipour, B., Wang, C.-M., Yuan, G., Teng, J., and Zheludev, N.I. (2016). Optically reconfigurable metasurfaces and photonic devices based on phase change materials. Nat. Photon. *10*, 60.

Wang, W., Shi, L., Zhao, R., Lim, K., Lee, H., Chong, T., and Wu, Y. (2008). Fast phase transitions induced by picosecond electrical pulses on phase change memory cells. Appl. Phys. Lett. *93*, 043121.

Wei, M., Song, Z., Deng, Y., Liu, Y., and Chen, Q. (2019). Large-angle mid-infrared absorption switch enabled by polarization-independent GST metasurfaces. Mater. Lett. *236*, 350–353.

West, P.R., Ishii, S., Naik, G.V., Emani, N.K., Shalaev, V.M., and Boltasseva, A. (2010). Searching for better plasmonic materials. Laser Photon. Rev *4*, 795–808.

Wuttig, M., Bhaskaran, H., and Taubner, T. (2017). Phase-change materials for non-volatile photonic applications. Nat. Photon. *11*, 465.

Xiao, S., Wang, T., Liu, T., Yan, X., Li, Z., and Xu, C. (2018). Active modulation of electromagnetically induced transparency analogue in terahertz hybrid metal-graphene metamaterials. Carbon *126*, 271–278.

Yin, X., Schäferling, M., Michel, A.-K.U., Tittl, A., Wuttig, M., Taubner, T., and Giessen, H. (2015). Active chiral plasmonics. Nano Lett. *15*, 4255–4260.

Zentgraf, T., Meyrath, T., Seidel, A., Kaiser, S., Giessen, H., Rockstuhl, C., and Lederer, F. (2007). Babinet's principle for optical frequency metamaterials and nanoantennas. Phys. Rev. B *76*, 033407.

Zhang, H., Cao, Y., Liu, Y., Li, Y., and Zhang, Y. (2017). A novel graphene metamaterial design for tunable terahertz plasmon induced transparency by two bright mode coupling. Opt. Commun. *391*, 9–15.

Zhang, L., Tang, Y., and Tong, L. (2019). Micro/nano fiber optics: merging photonics and material science on nanoscale for advanced sensing technology. iScience *23*, 100810.

Zhang, S., Genov, D.A., Wang, Y., Liu, M., and Zhang, X. (2008). Plasmon-induced transparency in metamaterials. Phys. Rev. Lett. *101*, 047401.

Zhong, Q., Wang, T., Jiang, X., Cheng, L., Yan, R., and Huang, X. (2020). Near-infrared multi-narrowband absorber based on plasmonic nanopillar metamaterial. Opt. Commun. *458*, 124637.

Zhou, X., Behera, J.K., Lv, S., Wu, L., Song, Z., and Simpson, R.E. (2017). Avalanche atomic switching in strain engineered Sb2Te3–GeTe interfacial phase-change memory cells. Nano Futures *1*, 025003.

Zhou, X., Kalikka, J., Ji, X., Wu, L., Song, Z., and Simpson, R.E. (2016). Phase-change memory materials by design: a strain engineering approach. Adv. Mater. *28*, 3007–3016.

Zhu, Y., Hu, X., Fu, Y., Yang, H., and Gong, Q. (2013). Ultralow-power and ultrafast all-optical tunable plasmon-induced transparency in metamaterials at optical communication range. Sci. Rep. *3*, 2338.

Supplemental Information

Tuning of Classical Electromagnetically

Induced Reflectance in Babinet

Chalcogenide Metamaterials

Kuan Liu, Yang Li, Kairong Qin, and Tun Cao

Transparent Methods

1 Fabrication

We chose the Si wafers as the substrates. Before the deposition, we cleaned the Si wafers ultrasonically in acetone, isopropanol and deionized water and dried the wafers by dry nitrogen. Afterwards, a 30 nm thick GST layer and a 40 nm thick Au layer were subsequently direct current magnetron sputter-deposited on the Si substrate. We deposited a Si_3N_4 buffer layer with a thickness of 5 nm on the GST layer at a 0.07 Å s^{-1} rate from a Si target at a 0.5 Pa pressure. We obtained the Si_3N_4 via reactively sputtering in an Ar: N_2 atmosphere of 8:2. The metamaterials were fabricated by a FEI Helios G4 UX focus ion beam (FIB) equipped with a Cobra FIB column and a five-channel gas injection system (GIS). Samples were cleaned by acetone and isopropanol and loaded into the FIB/SEM system. Spring coils were grown with Ga+ ion beam with a current of 41 pA and acceleration voltage of 30 keV. The step size was 10 nm to provide an excellent overlapping between two consecutive spots.

2 Measurements

We measured the reflectance of the Babinet metamaterials using a Fourier transform infrared (FTIR) spectrometer (IFS 66v/S) integrated with a Bruker IR microscope (Hyperion 2000). All spectroscopic data collected in transmission mode over the infrared region (4000-10000 cm^{-1}) with a spectral resolution of 3.8 cm^{-1}, which is achieved by a 15× infrared Schwarzschild objective by a liquid nitrogen-cooled MCT (mercury cadmium telluride) detector. We set the scanning velocity at 20 kHz. Interferograms are Fourier transformed with a Blackman-Harris 3-term apodization and a zero filling factor of 4. OPUS 6.0 software was employed to attain the spectral data. All FTIR spectra collected for the metamaterials are divided by the background spectra of a bare 100 nm Au film on the Si substrate to give a ratio of the reflectance output.

3 FDTD Simulations

A commercial software Lumerical Solutions based on the finite difference time-domain (FDTD) method was used to design the Babinet metamaterials. Periodic boundary condition is adopted in the *x-y* plane. In the *z*-axis, perfectly matched layer boundary condition is used to terminate the simulation field. A plane wave normally launched the metamaterials along the *z*-axis, and the reflectance is monitored by a power monitor locating 1000 nm above the metamaterials. A small square mesh (2 nm ×2 nm×2 nm) was taken to minimize the numerical error during the FDTD approximation. The numerical models take the tabulated, experimental permittivities for Au and Si that takes into account the losses. The complex permittivities of 30 nm thick GST films for the amorphous and crystalline states are measured by the VASE, which are subsequently fitted using Tauc-Lorentz models.